Cell Reports
Physical Science

CellPress
OPEN ACCESS

Article

The Effect of Anion Bridging on Heterogeneous Charge Transfer for V^{2+}/V^{3+}

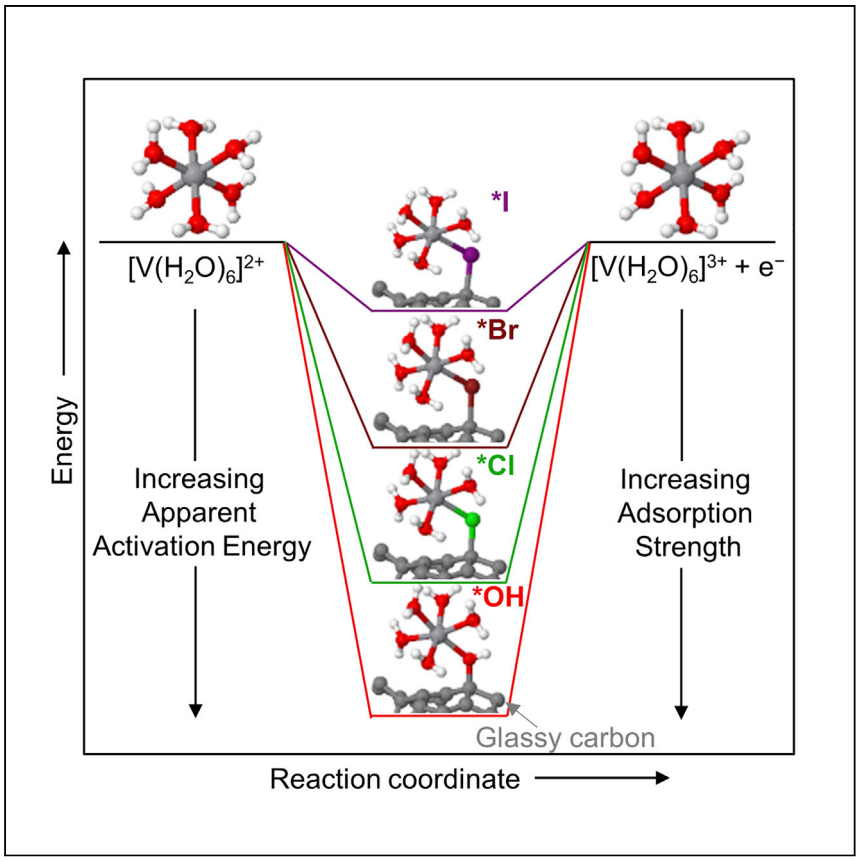

The slow V^{2+}/V^{3+} reaction in part limits vanadium redox flow battery commercialization. Agarwal et al. show that the V^{2+}/V^{3+} rate increases as the adsorption strength of the vanadium-anion intermediate decreases. The kinetic enhancement in the presence of different anions is not caused by changes in anion coverage. These findings also rationalize charge transfer kinetics for other transition metal ion redox couples.

Harsh Agarwal, Jacob Florian, Bryan R. Goldsmith, Nirala Singh

snirala@umich.edu

HIGHLIGHTS

V^{2+}/V^{3+} kinetics correlate with the energy of the adsorbed vanadium-anion intermediate

Energy of vanadium-anion intermediate correlates with free anion polarizability

Explains anion-induced enhancement seen for *3d* transition metal ion redox couples

Sulfate anion inhibits the V^{2+}/V^{3+} reaction kinetics

Agarwal et al., Cell Reports Physical Science 2, 100307
January 20, 2021
https://doi.org/10.1016/j.xcrp.2020.100307

Cell Reports
Physical Science

CellPress
OPEN ACCESS

Article

The Effect of Anion Bridging on Heterogeneous Charge Transfer for V^{2+}/V^{3+}

Harsh Agarwal,[1,2] Jacob Florian,[1,2] Bryan R. Goldsmith,[1,2,3] and Nirala Singh[1,2,4,5,*]

SUMMARY

Vanadium redox flow batteries suffer from inefficiencies partly due to the kinetics of the V^{2+}/V^{3+} reaction, for which lack of mechanistic understanding hinders electrolyte and electrocatalyst design to improve reaction rates. Here, we provide insights into the V^{2+}/V^{3+} reaction in $HClO_4$, H_2SO_4, HCl, HBr, and HI. We identify the V^{2+} and V^{3+} structures in these electrolytes using extended X-ray absorption fine structure, UV-vis, and density functional theory; this includes the hydrated structures of V^{2+} and V^{3+} in water (i.e., without anion complexation). We show that V^{2+}/V^{3+} kinetics correlate with the energy of vanadium intermediate bound to carbon through a bridging anion (*[bridge−V^{3+}]). The anion-induced kinetic enhancement is from a decreased activation energy because of changing *[bridge−V^{3+}] energy. The *[bridge−V^{3+}] energy increases in the order of anion polarizability ($OH^- < Cl^- < Br^- < I^-$), explaining previous reports that correlate anion polarizability with the kinetics of other 3*d* transition metal ion redox couples.

INTRODUCTION

Electrochemical charge transfer between metal ions in solution and electrode surfaces is relevant to corrosion,[1–3] metal electrodeposition,[4–6] chemical sensors,[7] and energy storage.[8–10] Electrochemical energy storage, with investments worth $1.3 billion in 2019,[11] is of ever increasing importance due to the growing use of intermittent renewable energy sources such as solar and wind.[12] A particularly relevant technology for grid-scale energy storage is the redox flow battery (RFB), which uses heterogeneous charge transfer to store and release energy.[9,10,13–15] Many RFBs using 3*d* transition metal ion redox couples in the aqueous phase have been demonstrated, and their efficiencies are dependent on the charge transfer kinetics occurring at the electrode.[14,16–20] These heterogeneous charge transfer reactions may occur by electron hopping without any bonding interaction between the reacting species and electrode (outer-sphere) or through adsorbed species on the electrode surface (inner-sphere). Outer-sphere charge transfer is described well by Marcus theory and its extensions.[21] Inner-sphere reactions are more complex and less understood due to the formation of adsorbed intermediates. Studying inner-sphere reactions at the molecular level can help identify electrode and electrolyte properties that govern the energetics of adsorbed intermediates on surfaces and how these affect the redox kinetics.

In this work, we study the link between electrolyte and adsorbed intermediates on the kinetics of the charge transfer reaction between vanadium (V) ions and a glassy carbon (GC) electrode. We select V^{2+}/V^{3+} as a model inner-sphere reaction both because it can serve to help us better understand inner-sphere charge transfer involving transition metal ions and its widespread use in RFBs. Although porous C

[1]Department of Chemical Engineering, University of Michigan, Ann Arbor, MI 48109-2136, USA

[2]Catalysis Science and Technology Institute, University of Michigan, Ann Arbor, MI 48109-2136, USA

[3]Twitter: @BryanRGoldsmith

[4]Twitter: @SinghLab_UMich

[5]Lead Contact

*Correspondence: snirala@umich.edu

https://doi.org/10.1016/j.xcrp.2020.100307

felts are the most common electrodes for the V^{2+}/V^{3+} reaction,[22] we use GC as the electrode surface due to its controlled electrochemical surface area and high conductivity. We identify the structures of the V ions in various electrolytes and show that the charge transfer is influenced by the structure of V ions and the anions present in the solution. By comparing our V^{2+}/V^{3+} results to previously reported Cr^{2+}/Cr^{3+},[23,24] Fe^{2+}/Fe^{3+},[25] and Cu^{+}/Cu^{2+} redox couples that have also been used for RFBs,[14,16,26] we observe similarities and hypothesize that the kinetic behavior of all of these redox couples can be explained by the adsorption energy of the metal-ion charge transfer intermediate. Thus, the results here rationalize the kinetic trends across a variety of RFB systems.

Despite being the most studied and well-developed RFB chemistry,[14] all-vanadium RFBs (VRFBs: $VO_2^{+}/VO^{2+}//V^{2+}/V^{3+}$) are in part still limited by slow charge transfer kinetics of reactions at the positive electrode (VO_2^{+}/VO^{2+}) and the negative electrode (V^{2+}/V^{3+}). The kinetic performance of these redox couples is highly dependent on the electrode surface.[27] As a result, there are mixed reports in the literature depicting either of the two redox couples as being slower on commonly used C electrodes.[22,28–33] Even though the use of V ions in both compartments eliminates cross-contamination,[14] the voltage losses arising from the slower kinetics lowers the overall round-trip electrical efficiencies of VRFBs. These lower-voltage efficiencies prevent VRFBs from reaching the US Department of Energy's (DOE) target for cost-competitive grid-scale energy storage.[34,35] Eliminating the V^{2+}/V^{3+} reaction overvoltage alone from existing VRFBs can increase their overall round-trip energy storage efficiency from 77% to ~86%.[36]

Elucidating the V^{2+}/V^{3+} charge transfer mechanism is crucial to aid in the development of electrodes and electrolytes to increase the V^{2+}/V^{3+} reaction kinetics and minimize the parasitic hydrogen evolution reaction (HER).[37] Faster V^{2+}/V^{3+} kinetics would also enable the use of thinner electrodes and decrease overvoltages from ohmic losses.[38] Ultimately, the increased kinetics and selectivity toward V^{2+}/V^{3+} would reduce the levelized cost of energy storage.[37,39]

The electrolyte plays a major role in V^{2+}/V^{3+} redox kinetics and overall VRFB performance. Full-cell VRFBs with C electrodes using HCl[40–42] or HCl/H_2SO_4 mixtures[43,44] perform better compared to H_2SO_4, which can arise due to the lowering of the ohmic overvoltage (increased conductivity), concentration overvoltage (lowered viscosity), and activation overvoltage (enhanced reaction kinetics).[45] We have recently shown by operating under kinetically limiting regimes that the kinetics of the V^{2+}/V^{3+} reaction in HCl are faster compared to H_2SO_4. The faster kinetics in HCl show that kinetics are in part responsible for higher current densities in these full-cell VRFBs.[46] Nevertheless, the reason for the kinetic enhancement and whether it is related to the structures of the V ions in these electrolytes is not well understood.

The V^{2+}/V^{3+} reaction on C is hypothesized to proceed via an inner-sphere mechanism involving an adsorbed V intermediate. The rate of V^{2+}/V^{3+} charge transfer depends on the amount of surface hydroxyl groups (*OH) on C,[47] and hence *OH groups are proposed to facilitate electron transfer from the adsorbed V to the electrode surface in H_2SO_4.[48,49] We showed that the V^{2+}/V^{3+} reaction on GC in H_2SO_4 or HCl is an inner-sphere reaction and hypothesized that it proceeds via an adsorbed anion acting as a bridge for electron transfer between the electrode and V complex (i.e., $*[bridge-V^{3+}]$; Scheme 1A).[46] The kinetic enhancement observed for V^{2+}/V^{3+} in HCl compared with H_2SO_4 can arise due either to a change in the energy of the adsorbed V intermediate (Scheme 1A) or an increase in anion coverage that increases the concentration of the active intermediate (Scheme 1B). That is, the enhancement

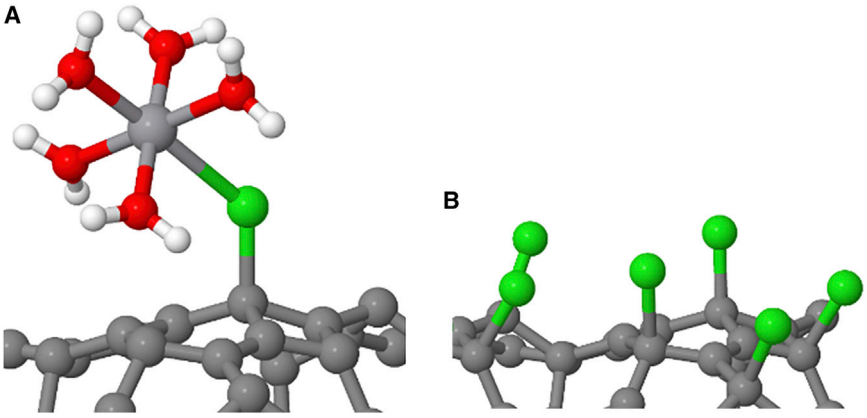

Scheme 1. Two Possible Causes for the Anion Effect on Charge Transfer Kinetics of Various Transition Metal Ion Redox Couples, Including V^{2+}/V^{3+} on Electrodes (e.g., Glassy Carbon [GC])

(A) Metal (M) ion complex adsorbed via an anion bridge (*[bridge–M]) whose energy controls the kinetics.

(B) Anion coverage controlling the concentration of active intermediates.

Atom color legend: dark gray = electrode (e.g., GC), light gray = metal (e.g., V), red = O, white = H, green = anion (e.g., chloride).

can be due to intrinsically faster charge transfer per active site or a higher number of active sites where charge transfer can occur.

The enhancement in kinetics observed for V^{2+}/V^{3+} in the presence of Cl^- is also seen for Cr^{2+}/Cr^{3+},[23,24] Fe^{2+}/Fe^{3+},[25] and Cu^{+}/Cu^{2+} redox couples on metal electrodes.[26] Moreover, the extent of kinetic enhancement for Cr^{2+}/Cr^{3+} on Hg electrodes follows the order $I^- > Br^- > Cl^- > OH^-$.[23] Anion coverage, which mirrors the order of kinetic enhancement, is one explanation used to rationalize the effect of anions on charge transfer in Cr^{2+}/Cr^{3+}, Fe^{2+}/Fe^{3+}, and Cu^{+}/Cu^{2+} redox couples.[23,50] An increased anion coverage (Scheme 1B) would affect the kinetics by increasing the concentration of active intermediates, resulting in a higher apparent frequency factor. The enhancement trend is also in the same order as increasing polarizability of the free anion (i.e., $I^- > Br^- > Cl^- > OH^-$); thus, the polarizability of the anion is also hypothesized to be a cause of this enhancement.[51–53] Although anion polarizability correlates with the enhancement in kinetics, it is unclear why polarizability of the anion would describe the kinetics of various transition metal ion redox couples considering that the anion polarizability is just the extent of electron cloud distortion in the presence of an electric field[52,54,55] and neither accounts for the presence of the electrode surface nor the metal ion involved.

Anions can affect the structure of the adsorbed intermediate or the metal ion complex in solution by entering the first coordination sphere. Therefore, rather than only considering anion polarizability or anion coverage (Scheme 1B), the metal ion itself should have a major effect on kinetics (Scheme 1A). Currently, the dearth of molecular-level understanding of the charge transfer pathway has made it difficult to explain how anions influence the redox kinetics for transition metal ions.

In this work, we reveal that the kinetic enhancement observed in chloride for the V^{2+}/V^{3+} reaction is due to a change in the energy of the adsorbed intermediate and not due to an increased anion coverage. The change in intermediate energy also explains the order of kinetic enhancement—i.e., iodide > bromide > chloride. The energy of this adsorbed intermediate follows the same order as the polarizability of the free anion. We postulate that a similar mechanism involving an adsorbed metal-ion

intermediate occurs for Cr^{2+}/Cr^{3+}, Fe^{2+}/Fe^{3+}, and Cu^{+}/Cu^{2+} redox couples. By understanding the cause of the enhancement for V^{2+}/V^{3+}, we also increase our understanding for these other redox couples that are used in a range of RFBs.[14,16]

The challenge in understanding the role of anions on the kinetics and charge transfer mechanism of metal ion redox couples arises from four shortcomings in the literature: (1) rates are not always measured under kinetic control and are often not normalized by electrochemical active surface area; (2) apparent activation energies (E_a) and frequency factors are not evaluated, which makes it difficult to know whether kinetic enhancement is related to lowered activation energy of the rate determining step (RDS) or increased coverage; (3) the structure of the reacting species in different electrolytes is not known under electrochemical conditions; and (4) first-principles modeling has not been used to understand the influence of anion coverage and adsorption strength of the intermediates on charge transfer. We address these four shortcomings in the literature, focusing on the V^{2+}/V^{3+} redox couple, with a combined experimental and computational study. This combined analysis enables us to understand the energetics of the adsorbed intermediate and propose a reaction mechanism that explains the kinetics of V^{2+}/V^{3+} in all of the tested electrolytes.

We demonstrate in this work by operating under kinetically limiting regimes that the exchange current densities (i_o) of the V^{2+}/V^{3+} reaction on GC increase following the order H_2SO_4 < HCl < $HClO_4$ < HBr < HI, with the E_a following the order H_2SO_4 > $HClO_4$ > HCl > HBr > HI. The reaction kinetics in a mixture of HI/H_2SO_4 is close to that of pure H_2SO_4, which we attribute to SO_4^{2-} preventing the formation of the active intermediate responsible for the high activity in HI. The decrease in E_a for V^{2+}/V^{3+} occurs in the order of the increasing polarizability of the anion that forms the bridge for electron transfer. However, the apparent frequency factor, which is proportional to the coverage of the active intermediate, follows an order that is the opposite of the DFT-predicted anion coverages. This contradiction suggests that the kinetic enhancement does not result from higher anion coverage.

We use extended X-ray absorption fine structure spectroscopy (EXAFS), molecular dynamics EXAFS (MD-EXAFS), UV-vis spectroscopy, and ligand-exchange free energy (ΔG_L) calculations to identify the structures of V^{2+} and V^{3+} in these five electrolytes. We in particular report the structures of V^{2+} and V^{3+} in commercially used H_2SO_4 and HCl using EXAFS. V^{2+} exists in hydrated form as $[V(H_2O)_6]^{2+}$ in all of the electrolytes, whereas V^{3+} complexes with anions. We find that the V^{2+}/V^{3+} reaction kinetics increases with decreasing adsorption strength of the *[bridge–V^{3+}] intermediate (i.e., increase in energy of the intermediate). This finding is supported by a postulated mechanism that fits the observed experimental behavior.

We postulate the adsorption strength of the intermediate, similar to V^{2+}/V^{3+}, can be used to control the heterogeneous charge transfer for other reactions that obey a similar anion-bridging mechanism such as Cr^{2+}/Cr^{3+}, Fe^{2+}/Fe^{3+}, and Cu^{+}/Cu^{2+}. The structure of the reacting species, the identity of the anions, and the electrode surface affect the energetics of the formed intermediate and should be considered when interpreting inner-sphere charge transfer kinetics.

RESULTS AND DISCUSSION

V^{2+}/V^{3+} Reaction Kinetics on GC

We report the i_o, reaction orders, and E_a for the V^{2+}/V^{3+} reaction on GC in five acidic electrolytes obtained from steady-state current (Tafel method) and impedance

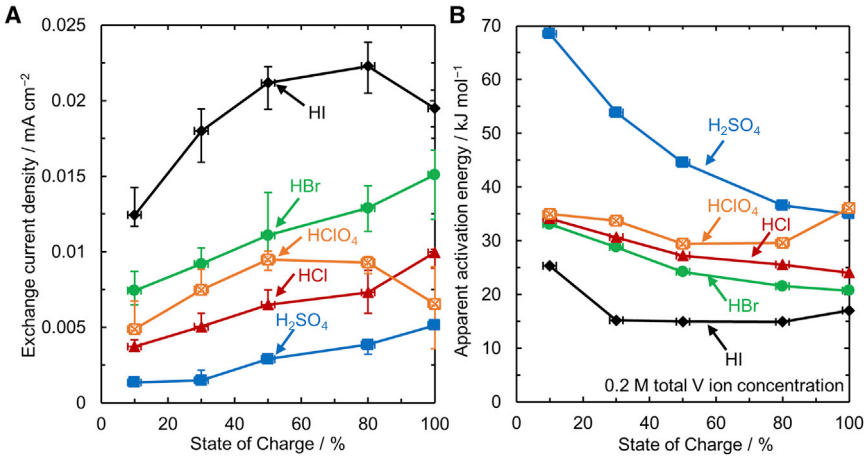

Figure 1. Kinetic Parameters for V^{2+}/V^{3+} Reaction in Various Acidic Electrolytes

Exchange current densities (A) and apparent activation energies (B) as a function of state of charge for the V^{2+}/V^{3+} redox reaction evaluated from the Tafel method in 1 M HI, 1 M HBr, 1 M $HClO_4$, 1 M HCl, and 0.5 M H_2SO_4 at 0.2 M total vanadium (V) ion concentration. The values for H_2SO_4 and HCl are adapted from Agarwal et al.[46] The exchange current densities are unchanged in 1 M H_2SO_4 in comparison to 0.5 M H_2SO_4. The counter electrolyte is $HClO_4$ instead of H_2SO_4 for studying HI to prevent contamination from SO_4^{2-} crossing through the membrane. The H^+ ion concentration in the electrolyte in the counter electrode compartment is the same as that of the working electrolyte. The error bars on the exchange current densities and states of charge are the standard deviations of the average values.

measurements (charge transfer resistance method). The use of these two independent methods assists with ensuring reproducibility and also provides information to discern the total number of electrons involved in the reaction.[46] Our experimental protocol is discussed in the Supplemental Experimental Procedures.

The data in Figure 1 shows that the V^{2+}/V^{3+} reaction kinetics varies with state of charge (SoC), (SoC = $[V^{2+}]/([V^{2+}] + [V^{3+}])$), in $HClO_4$, HBr, and HI, similar to HCl and H_2SO_4 reported previously.[46] The SoC is measured by evaluating the concentration of V^{2+} and V^{3+} using UV-vis (Figures S1–S4; Tables S1 and S2). The i_o increases (Figure 1A) and the E_a decreases (Figure 1B) with increasing SoC in HBr, HCl, and H_2SO_4. However, the i_o displays a maximum (and minimum in E_a) between 50% and 80% SoC in $HClO_4$ and HI. The i_o are evaluated in the kinetically limiting regime (Figure S5) using the oxidation currents to prevent contributions from HER (Figure S6). Because i_o does not vary with increasing rotation rates, these measurements are under the kinetically limiting regime (Figure S5). We also confirmed that the choice of the reference electrode did not affect the measured V^{2+}/V^{3+} kinetics (Figure S7), which is highlighted as an important concern for electrochemical reactions due to possible impurities.[56]

By comparing i_o evaluated using the Tafel method ($i_{o,Tafel}$) and charge transfer resistance method ($i_{o,R_{ct}}$) using Equation S12, we show that the V^{2+}/V^{3+} reaction is an overall two-electron transfer reaction with one electron in the RDS in HBr, the same as in HCl (Figure S8; Table S3). In contrast, the V^{2+}/V^{3+} reaction is overall one-electron transfer in $HClO_4$ and HI (Figure S9; Table S3), the same as in H_2SO_4. This overall two-electron transfer behavior observed in HCl and HBr may arise either due to the formation of V dimers on the electrode surface, a comproportionation reaction between adsorbed V^{2+} and V^{4+} on the surface to form V^{3+},[46,57] or the partial charge transfer from halide when V di-halide (chloride and bromide) complexes are

Table 1. Reaction Orders for V^{2+}/V^{3+} in H_2SO_4 and HI

	$[V^{2+}]$ Order (γ)		$[V^{3+}]$ Order (ε)	
Electrolyte	$i_{o,Tafel}$	$i_{o,R_{ct}}$	$i_{o,Tafel}$	$i_{o,R_{ct}}$
H_2SO_4	0.25	0.22	−0.25	−0.23
HI with $HClO_4$ on counter electrode	0.67	0.68	0.28	0.32

The orders are calculated from exchange current densities at different total vanadium (V) concentrations (0.05, 0.1, and 0.2 M V) at room temperature using regression.

formed in solution. Despite the difference in the overall number of electrons, the Tafel slopes (b) in all of these electrolytes range from 120 to 150 mV decade^{-1} (Figure S10), corresponding to a RDS with one-electron transfer.

Because i_o includes the contribution of both apparent frequency factor and E_a, we measure both i_o and E_a to understand how anions influence the kinetics. These measurements enable us to distinguish whether the kinetic enhancement is related to the apparent frequency factor or E_a. The i_o of the V^{2+}/V^{3+} reaction in these electrolytes increases following the order of H_2SO_4 < HCl < $HClO_4$ < HBr < HI. The E_a decreases in the order of $HClO_4$ > HCl > HBr > HI and follows the same order as the anion polarizability (OH^- < Cl^- < Br^- < I^-). The decreasing E_a with increasing anion polarizability implies that an adsorbed V species with an anion bridge may act as an intermediate in the overall charge transfer mechanism. The i_o in $HClO_4$ is higher compared with HCl (Figure 1A), despite its higher E_a (Figure 1B) because the i_o contains contributions from the apparent frequency factor in addition to E_a. The i_o in various electrolytes at different temperatures along with Arrhenius plots to evaluate E_a are shown in Figures S12–S14 and Table S4. We hypothesize the slow kinetics in H_2SO_4 arise from SO_4^{2-} preventing the formation of an active intermediate, because SO_4^{2-} cannot act as a bridge for charge transfer reactions.[58]

To clarify the reaction mechanism, the reaction orders of V^{2+} and V^{3+} in different electrolytes are extracted by regression analysis on i_o and are given in Table 1. Details on this analysis are discussed in the Supplemental Experimental Procedures. No dependence on the total V concentration in H_2SO_4 was shown in our previous work, and the behavior with SoC was explained by V^{2+} and V^{3+} having equal and opposite reaction orders (i.e., a positive order for V^{2+} and a negative order for V^{3+}).[46] Reaction orders evaluated in H_2SO_4 here (Table 1) corroborate this finding. Due to the same qualitative trend in i_o (and E_a) with SoC in HCl and HBr (Figure 1) as in H_2SO_4, the V^{2+} and V^{3+} orders in HCl and HBr are also evaluated assuming they are equal and opposite (Figure S15; Table S5). In contrast, both V^{2+} and V^{3+} have positive orders in HI (Table 1; Figures S16 and S17) and $HClO_4$ (Table S5), which explains the maxima observed in i_o around 50%–80% SoC in Figure 1. The orders of V^{2+} and V^{3+} in HI evaluated by the differential method (Supplemental Experimental Procedures) qualitatively corroborate the orders obtained by regression (Figures S18 and S19; Table S6). Although an outer-sphere reaction rationalizes the positive orders for both V^{2+} and V^{3+} in $HClO_4$ and HI, an outer-sphere reaction cannot describe the observed negative reaction order of V^{3+} in H_2SO_4, HCl, and HBr (Supplemental Experimental Procedures). Therefore, we choose a single inner-sphere reaction mechanism described below that explains the reaction order behavior in all of the electrolytes.

The experimental V^{2+}/V^{3+} rate measurements in these electrolytes can be explained by a simple inner-sphere microkinetic model involving adsorbed V through an anion bridge as an intermediate (Scheme 1A):

$$V^{2+} + * \rightleftarrows *V^{2+} \qquad \text{(Step 1)}$$

$$* V^{2+} \rightleftarrows * V^{3+} + e^- \quad \text{(Step 2)}$$

$$* V^{3+} \rightleftarrows V^{3+} + * \quad \text{(Step 3)}$$

Here * represents a GC active site, which is either free or occupied by a reactive species. The i_o, assuming the single electron transfer in step 2 is the RDS (based on the measured Tafel slopes; Figure S10), can be written as (see derivation in Supplemental Experimental Procedures):

$$i_o = \frac{nFk_oK_1[V^{2+}]}{(K_1[V^{2+}] + K_3[V^{3+}] + 1)}\left(\frac{[V^{3+}]}{[V^{2+}]}\right)^{\left(\frac{n_k(1-\alpha)}{n}\right)} \quad \text{(Equation 1)}$$

where F = Faraday's constant, α = the transfer coefficient, n_k = the number of electrons involved in the RDS (i.e., 1), n = the total number of electrons involved in the reaction, k_o = the standard rate constant for step 2 (i.e., rate constant at the V^{2+}/V^{3+} standard redox potential), and K_1 and K_3 are the adsorption constants for V^{2+} and V^{3+}, respectively.

A reaction model involving an adsorbed anion (Scheme 1B) can also explain the observed reaction orders of V^{2+} and V^{3+} in all of the electrolytes (Supplemental Experimental Procedures), with the reaction kinetics proportional to the coverage of anions on the electrode surface.[23,50] Although the mechanisms associated with Schemes 1A and 1B both explain the observed reaction orders, we discuss further evidence to distinguish them below. Because the only evidence of an overall two-electron transfer reaction is the comparison of $i_{o,Tafel}$ and $i_{o,R_{ct}}$, and there is a lack of spectroscopic evidence of an adsorbed surface intermediate, we choose a simple reaction model involving overall one-electron transfer (in RDS), consistent with the observed Tafel slopes (Figure S10) in all of the electrolytes studied here. More complex multi-step reaction mechanisms could also describe the observed kinetic behavior, but we choose these two basic models to follow the principle of Occam's razor.[59]

We also investigate the V^{2+}/V^{3+} reaction kinetics in mixtures of anions to understand the relative energy of the formed intermediates and the anion coverage. We expect the largest difference in the adsorption energy or concentration of the active intermediate between the electrolytes that have the largest difference in observed kinetics. Thus, we study the V^{2+}/V^{3+} kinetics in a mixture of I^- (highest activity) and SO_4^{2-} (lowest activity) in the following section. If the V-sulfate intermediate is lower in energy than the V-iodide intermediate, or the coverage of SO_4^{2-} is higher than I^- on GC, then the kinetics in the HI/H_2SO_4 mixture will be more similar to H_2SO_4 than HI, and vice versa.

Influence of Sulfate Anions on V^{2+}/V^{3+} Reaction Kinetics

We observe that the presence of sulfate/bisulfate (SO_4^{2-}/HSO_4^-) decreases the V^{2+}/V^{3+} kinetics in HI. The i_o in HI with H_2SO_4 in the counter electrode (CE) compartment is much lower in comparison with non-interacting $HClO_4$ in the CE compartment (Figure 2A) and nearly matches the i_o in pure H_2SO_4 at the same SoC, shown by the flat solid line in Figure 2A. In our experimental setup (see Supplemental Experimental Procedures), we use a Nafion-117 proton-exchange membrane to separate cell compartments. We hypothesize that SO_4^{2-}/HSO_4^- anions cross through the membrane and suppress the kinetics. The data in Figure 2A support this hypothesis, because the V^{2+}/V^{3+} kinetics decrease upon increasing the amount of $NaHSO_4$ in HI, even with $HClO_4$ in the CE compartment. At sufficiently high $NaHSO_4$

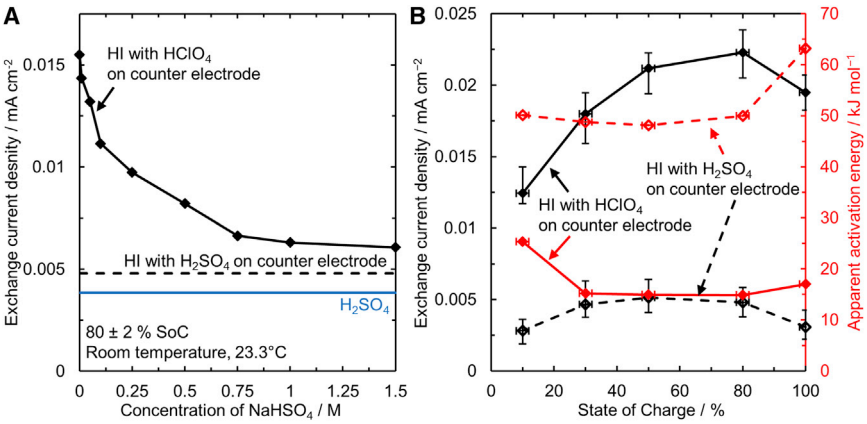

Figure 2. Influence of Sulfate on V^{2+}/V^{3+} Kinetics in HI

(A) Exchange current densities at 80% ± 2% state of charge for V^{2+}/V^{3+} reaction in 1 M HI with 1 M $HClO_4$ in CE compartment with increasing concentrations of $NaHSO_4$. The solid and dashed horizontal lines show the baseline exchange current densities in 0.5 M H_2SO_4 and 1 M HI with 0.5 M and 1 M H_2SO_4 in the CE compartment, respectively.

(B) Exchange current densities and apparent activation energies for V^{2+}/V^{3+} reaction in 1 M HI with 1 M $HClO_4$ (solid) and 1 M H_2SO_4 (dashed) in the CE compartment. The error bars on the exchange current densities and states of charge are the standard deviations of the average values.

concentrations, the i_o is comparable to the case of HI with H_2SO_4 in the CE compartment. Even though the perchlorate anion will also cross over to the working electrode compartment when using $HClO_4$ in the CE compartment, the kinetics in HI will be unaffected because of the non-interacting nature of perchlorate to complex with V ions, contrary to the case of H_2SO_4 in the CE compartment. This effect of SO_4^{2-} suppressing the reaction kinetics is qualitatively captured by the larger E_a and smaller i_o for reaction in HI with H_2SO_4 compared to $HClO_4$ in the CE compartment (Figure 2B). The E_a in HI with H_2SO_4 in the CE compartment is comparable to that in pure H_2SO_4.

These results, that SO_4^{2-} decreases the V^{2+}/V^{3+} kinetics, suggest that SO_4^{2-} prevents the formation of the active intermediate in HI. This kinetic inhibition may occur from adsorbed V-sulfate complexes preventing the formation of active V-iodide complexes or adsorbed sulfate blocking the adsorption of I^-. Understanding the reason for this catalytic inhibition requires knowledge of the structures of the V species at the surface and the coverage of anions. To accomplish this task, we experimentally determine the structures of the species in solution and then use DFT modeling to understand the interaction of species on the C surface and the effect of anion coverage in the next sections.

Structures of V^{2+} and V^{3+} in $HClO_4$, H_2SO_4, and HCl, Using EXAFS and MD-EXAFS

We use *in situ* EXAFS measurements and MD-EXAFS of the V K-edge to elucidate the structures of V ions in $HClO_4$, H_2SO_4, and HCl. We electrochemically control the oxidation state of V in these electrolytes as either V^{2+} or V^{3+} during the measurements to prevent any contamination from undesired oxidation to higher oxidation states. MD-EXAFS are computed by averaging the EXAFS spectra generated from *ab initio* MD snapshots of V complexes in explicit solvent.[60] We use 50 solvent water molecules in the MD-EXAFS simulations and show that increasing the number of solvent molecules does not change the MD-EXAFS spectra (Figure S20). All of the computational details for the MD-EXAFS are provided in the Supplemental

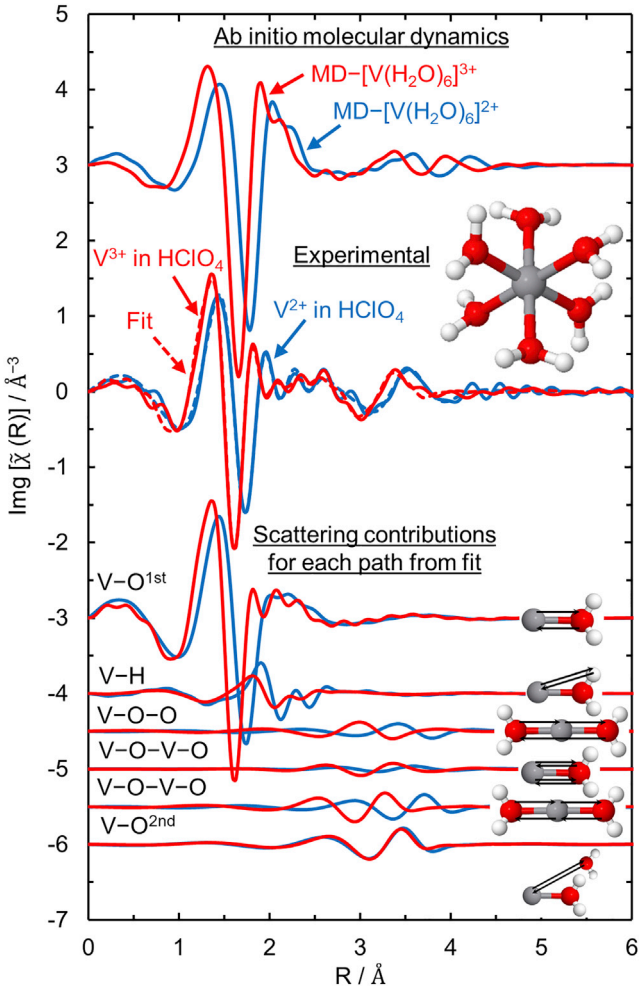

Figure 3. Structures of Hydrated V^{2+} and V^{3+}

The k^2-weighted Img[$\tilde{\chi}$(R)] plots for MD-EXAFS of V complexes in pure water—that is, $[V(H_2O)_6]^{2+}$ (blue) and $[V(H_2O)_6]^{3+}$ (red). Below the MD-EXAFS are the experimental V K-edge EXAFS of V^{2+} (blue) and V^{3+} (red) in perchloric acid. The fit is shown by the dotted lines. The individual scattering paths that are used in the structural refinement are shown, along with their contributions in the resulting fit. Atom color legend: light gray = V, red = O, and white = H.

Experimental Procedures. By using both experimental EXAFS and MD-EXAFS, we are confident in attributing certain features of the spectra to specific V complexes. We begin by identifying the structures of V species in the absence of anion complexation by conducting EXAFS measurements in non-complexing perchloric acid. The structural parameters in $HClO_4$ serve as a standard to identify complexed species in H_2SO_4 and HCl.

The data at the top of Figure 3 shows the Img[$\tilde{\chi}$(R)] plots of hydrated $[V(H_2O)_6]^{2+}$ and $[V(H_2O)_6]^{3+}$ obtained from MD-EXAFS. Below the MD-EXAFS of $[V(H_2O)_6]^{2+}$ and $[V(H_2O)_6]^{3+}$ are the experimental EXAFS of V^{2+} and V^{3+} in $HClO_4$, where V^{2+} and V^{3+} are expected to be hydrated due to the non-interacting nature of perchlorate.[61,62] The MD-EXAFS of $[V(H_2O)_6]^{2+}$ and $[V(H_2O)_6]^{3+}$ match the dominant features of the first coordination sphere (<3 Å) of the experimental measurements. Both MD-EXAFS and EXAFS show a shorter scattering distance of the first coordination sphere for V^{3+} compared to V^{2+}. The agreement between the MD-EXAFS and

experimental EXAFS suggests that V^{2+} and V^{3+} exist in fully hydrated form in $HClO_4$. These results provide direct experimental verification of the V^{2+} and V^{3+} structures in water. No previous studies have accurately elucidated the structures of hydrated V^{2+} and V^{3+} complexes in the aqueous phase. Although a previous study on the structure of hydrated V^{3+} in the aqueous phase has been conducted, the V^{3+} solution used contained chloride anions along with concentrations of V^{4+}, as seen by their UV-vis spectra of the prepared solution.[63] The structural parameters of hydrated V^{2+} and V^{3+} we see here agrees with the *ab initio* calculations and experimental X-ray and neutron diffraction studies of solid $VSO_4 \cdot 6H_2O$ and $[V(H_2O)_6][H_5O_2](CF_3SO_3)_4$ crystals.[61,62,64–66] The k^2-weighted EXAFS spectra of V^{2+} and V^{3+} in perchloric acid in R and k space are available in Figures S21 and S22.

By fitting the EXAFS data, we identify the scattering paths that contribute to the different portions of the overall EXAFS spectra. We quantify distances of scattering paths for both V^{2+} and V^{3+} in perchloric acid and compare them to the MD-EXAFS values. The individual path contributions obtained by fitting are shown at the bottom of Figure 3. The single leg scattering from the first shell (V-O and V-H) dominates the scattering in the region from 1−2 Å. The multiple leg scatterings (V-O-O: 3-leg collinear path, V-O-V-O: double return and 4-leg collinear path) in the region from 2 to 4 Å are sensitive to first-shell symmetry and disorder. The paths used in the fit are based on previous studies for hydrated transition metal ions (Table S7) and are discussed in the Supplemental Experimental Procedures.[67] The V-O distance from experimental EXAFS of V^{2+} is 2.14 Å, while it is 2.0 Å for V^{3+}, within 0.01 Å of the previously reported V-O distances for V^{2+} and V^{3+} in $VSO_4 \cdot 6H_2O$ and $[V(H_2O)_6][H_5O_2](CF_3SO_3)_4$ crystals.[64–66] From MD-EXAFS, the V-O distance in V^{2+} and V^{3+} is 2.21 and 2.08 Å, respectively, within 0.05 Å of the previously reported V-O distances for V^{2+} and V^{3+} from electronic structure calculations.[62] The fitting parameters for all single leg scattering paths are available in Table S10, and details of the measurements and parameters of multileg scattering paths are available in the Supplemental Experimental Procedures. Using the structures of V^{2+} and V^{3+} and the associated scattering paths in non-complexing solution, we will be able to identify the structures in different electrolytes by comparing their spectra to these standards.

The UV-vis spectra of V^{2+} are unaffected by the presence of different anions (SO_4^{2-}, Cl^-, Br^-, and I^-, as shown in Figure S1), indicating that V^{2+} is present as $[V(H_2O)_6]^{2+}$ in all of the electrolytes.[46] Therefore, we assume that the structural properties of V^{2+} in all of the electrolytes studied here are the same as in $HClO_4$, shown in Figure 3. Unlike V^{2+}, the UV-vis spectra of V^{3+} is different in the presence of interacting anions in solution (Figure S1),[46,68–72] indicating a change in the first-coordination sphere. The UV-vis peak of V^{3+} corresponding to the $^3T_{1g} \rightarrow {}^3T_{2g}$ transition[73,74] shifts from that in non-complexing $HClO_4$ most significantly in H_2SO_4, followed by HCl, HBr, and then least in HI (Figure S4).[46] As this shift is attributed to complexation, the anion complexation strength of V^{3+} follows this same order, which matches the spectrochemical series that provides an estimate of the strength of ligand interaction with transition metals (ligand strength: $SO_4^{2-} >> Cl^- > Br^- > I^-$).[58] However, the exact structural changes of V^{3+} in the presence of anions have not been identified in the aqueous phase. To identify the structures of V^{3+} complexes in H_2SO_4 and HCl, we conducted *in situ* EXAFS measurements of V^{3+} in H_2SO_4 and HCl with increasing anion concentrations and compared them to the EXAFS of V^{3+} in $HClO_4$. Because weaker complexation of V^{3+} with Br^- and I^- than Cl^- and SO_4^{2-} is predicted by the spectrochemical series[58] and corroborated by our UV-vis measurements,[46] we rely on DFT-calculated ΔG_L (Table S11; Supplemental

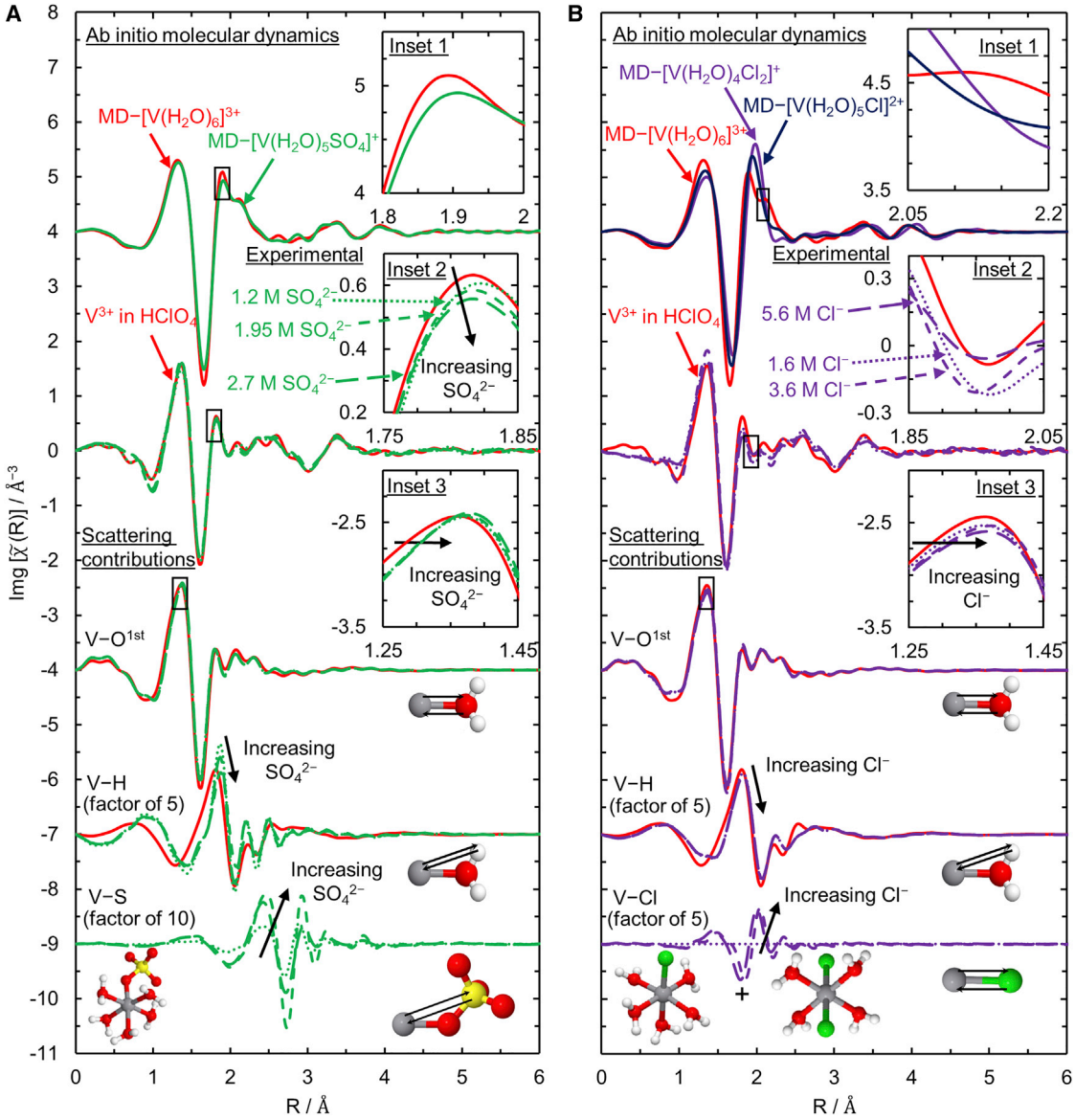

Figure 4. Structure of V^{3+} in H_2SO_4 and HCl with Changing Anion Concentrations

The V K-edge EXAFS k^2-weighted Img[$\tilde{\chi}$(R)] plots for V^{3+} with increasing concentrations of (A) SO_4^{2-} and (B) Cl^- anions compared with the case of hydrated V^{3+} ion in perchloric acid. The experimental spectrum is compared with the MD-EXAFS of $[V(H_2O)_5SO_4]^+$ in H_2SO_4, and $[V(H_2O)_5Cl]^{2+}$ and $[V(H_2O)_4Cl_2]^+$ in HCl, along with the hydrated V^{3+} ion (i.e., $[V(H_2O)_6]^{3+}$). The insets show the similarity in the relevant EXAFS region that are used to identify the presence of complexes in solutions at different concentration of anions. The contribution of the V-O, V-H, and V-S paths (in A), and V-Cl paths (in B) that are used in structural refinement are compared to the contribution of each of these paths in hydrated V^{3+}, obtained by fitting in Artemis. The contribution of V-H, V-S, and V-Cl paths are multiplied by a scaling factor to highlight the trends. Atom color legend: light gray = V, red = O, white = H, yellow = S, and green = chloride.

Experimental Procedures) to identify the preferred complex in HBr and HI, rather than EXAFS measurements.

The data in Figure 4A provide evidence of V^{3+} complexation in H_2SO_4. The top of Figure 4A plots the Img[$\tilde{\chi}$(R)] of $[V(H_2O)_5SO_4]^+$ and $[V(H_2O)_6]^{3+}$ obtained by MD-EXAFS. There is a decline in the peak amplitude between 1.8 and 2.0 Å (inset 1, Figure 4A) with the introduction of SO_4^{2-} in the first coordination sphere. The same peak occurs between 1.75 and 1.85 Å in the experimental EXAFS of V^{3+} in H_2SO_4, where we

observe that the peak amplitude decreases with increasing SO_4^{2-} concentration (inset 2, Figure 4A), which we attribute to the presence of $[V(H_2O)_5SO_4]^+$.

We fit the EXAFS data to determine the change in the contribution of individual paths for V^{3+} with increasing SO_4^{2-}. The fittings are done considering an additional V-S single leg scattering path, as shown in Figure 4A, in addition to the paths used for fittings in perchloric acid shown in Figure 3. The fits and details of structural parameters used are available in Table S8. In sulfuric acid, the V-O path is shifted to the right (inset 3, Figure 4A), with a change in the V-O distance in H_2SO_4 relative to $HClO_4$ (Table S10). The change in the average V-O distance with SO_4^{2-} complexation occurs due to an increasing contribution of the V-O bond (with O between V and S in sulfate anion). Furthermore, at the bottom of Figure 4A, the increasing contribution of the V-S path and decreasing contribution of the V-H scattering path confirm increased V^{3+} complexation with SO_4^{2-} at higher SO_4^{2-} concentrations. This increased V^{3+} complexation is quantified by the increase in the average coordination number of the V-S path with increasing SO_4^{2-} concentration (Table S10). Therefore, V^{3+} exists as a mixture of $[V(H_2O)_5SO_4]^+$ and $[V(H_2O)_6]^{3+}$ in H_2SO_4, supporting our previous hypothesis by UV-vis spectroscopy.[46]

Our experimental EXAFS of V^{3+} in HCl shows clear evidence of Cl^- complexation, and by comparing to the MD-EXAFS $Img[\tilde{\chi}(R)]$ plots of $[V(H_2O)_5Cl]^{2+}$, $[V(H_2O)_4Cl_2]^+$, and $[V(H_2O)_6]^{3+}$ (Figure 4B), we see that both mono- and di-chloride V^{3+} complexes exist in HCl. The differences in experimental EXAFS are more subtle in HCl than in H_2SO_4 due to weaker complexation with Cl^- than SO_4^{2-}. The amplitudes of the peaks and troughs in the first coordination sphere of V^{3+} either monotonically increase or decrease with increasing Cl^- coordination in MD-EXAFS and Cl^- concentration in experimental EXAFS. However, for the amplitude of the feature between 2.05 and 2.20 Å in MD-EXAFS, the order is not monotonic, but instead $[V(H_2O)_6]^{3+} > [V(H_2O)_4Cl_2]^+ > [V(H_2O)_5Cl]^{2+}$ (inset 1, Figure 4B). This same feature as identified in MD-EXAFS occurs between 1.85 and 2.05 Å in experimental EXAFS (inset 2, Figure 4B), where the amplitude first decreases and then increases with increasing Cl^- concentration. This switch in order is not possible if only higher concentrations of $[V(H_2O)_5Cl]^{2+}$ are formed with increasing Cl^- concentration, indicating the presence of detectable concentrations of $[V(H_2O)_4Cl_2]^+$ along with $[V(H_2O)_5Cl]^{2+}$ at high concentrations of Cl^-.

We fit the EXAFS spectra of V^{3+} in HCl and deconvolute the contribution due to Cl^- complexation by including an additional single leg V-Cl scattering path during fitting as shown in Figure 4B, with fitting details in Table S9. The V-O path contribution moves toward the right (inset 3, Figure 4B) in HCl relative to $HClO_4$. Furthermore, at the bottom of Figure 4B, the increasing contribution of the V-Cl path and decreasing contribution of the V-H scattering path with increasing Cl^- concentrations confirm V^{3+} complexation. The increasing coordination number of V-Cl with increasing Cl^- (Table S10) provide an estimate of the average number of anions in the first coordination sphere of V^{3+}. The V-Cl path is not included in fitting in 1.6 M Cl^- because introducing a V-Cl path worsened the obtained fits, indicating negligible complexation. We observe that the V-Cl distance is larger than the V-O distance, which we attribute to Jahn-Teller distortion in $[V(H_2O)_5Cl]^{2+}$ and $[V(H_2O)_4Cl_2]^+$ formed in HCl.[58] Therefore, V^{3+} exists predominantly as $[V(H_2O)_6]^{3+}$ with small concentrations of $[V(H_2O)_5Cl]^{2+}$ and $[V(H_2O)_4Cl_2]^+$ in HCl. The EXAFS analysis of the V^{3+} complex in HCl provides evidence of the formation of $[V(H_2O)_4Cl_2]^+$ hypothesized from UV-vis in our previous work.[46] The presence of $[V(H_2O)_4Cl_2]^+$ may also be related to the overall two-electron transfer behavior observed in HCl.

We were unable to identify the presence of V dimers in the electrolytes studied by EXAFS. The absence of any intense peak ~3.1 Å (Figures S21–S24) attributed to V-V scattering in previous studies confirms the absence of dimers in our electrolytes.[75–77] The absence of dimers is also corroborated by UV-vis spectroscopy, which does not show any new transition peaks[76] or shoulders in the existing transition peaks with varying V^{3+} concentrations (Figure S1).[46] However, the formation of V dimers, comproportionation reaction between V^{2+} and V^{4+} on the surface,[46,57] or the V di-halide complexes could explain the overall two-electron transfer behavior observed in HCl and HBr. The presence of V dimers and V^{4+} on the surface can be identified by surface probing techniques such as *in situ* Raman spectroscopy and nuclear magnetic resonance, which is beyond the scope of this work. Since we have no direct evidence of V^{2+}/V^{3+} being a two-electron transfer reaction in HCl and HBr apart from comparing $i_{o,Tafel}$ and $i_{o,R_{ct}}$, we choose a simple reaction mechanism to avoid speculation.

$[V(H_2O)_5Br]^{2+}$ and $[V(H_2O)_4Br_2]^{+}$ are formed in HBr and $[V(H_2O)_5I]^{2+}$ and $[V(H_2O)_4I_2]^{+}$ are formed in HI, but in even lower concentrations than the V^{3+}-chloride complexes in HCl. Our prediction of the presence of these complexes is based on the exergonic DFT-calculated ΔG_L for $[V(H_2O)_5X]^{2+}$ and $[V(H_2O)_4X_2]^{+}$ (X = Cl, Br) from $[V(H_2O)_6]^{3+}$. Even though the ΔG_L of $[V(H_2O)_5I]^{2+}$ and $[V(H_2O)_4I_2]^{+}$ are slightly endergonic, we expect some of the V^{3+}-iodide complexes to form in solution based on changes in UV-vis with increasing I^- concentrations (Figure S4). The di-halide V^{3+} complex (X = Cl, Br) is more favorable than the mono-halide V^{3+} complex in HCl and HBr, while the mono-iodide V^{3+} complex is more favorable than the di-iodide V^{3+} complex, matching the overall two- versus one-electron transfer observed in HCl and HBr compared to HI (Supplemental Experimental Procedures). With the kinetic information combined with the V structural information in the five electrolytes, we propose a microkinetic model in the following section.

Proposed Inner-Sphere Mechanism and Kinetic Model for V^{2+}/V^{3+} Reaction in Different Electrolytes

The i_o (Equation 1) is simplified for three possible limiting conditions, depending on the values of the V^{2+} and V^{3+} adsorption constants, yielding an expression of the form:

$$i_o = A \exp\left(-\frac{E_a}{RT}\right)\left[V^{2+}\right]^{\gamma}\left[V^{3+}\right]^{\varepsilon} \qquad \text{(Equation 2)}$$

When measuring i_o as a function of T and creating an Arrhenius plot, $A[V^{2+}]^{\gamma}[V^{3+}]^{\varepsilon}$ is the apparent (experimentally observed) frequency factor, γ and ε are reaction orders of V^{2+} and V^{3+}, respectively, and E_a is the apparent activation energy.

If $K_3[V^{3+}] >> (1 + K_1[V^{2+}])$, that is, V^{3+} adsorbs strongly and much stronger than V^{2+}, then at a given temperature, $i_o \propto [V^{2+}]^{(1-n_k(1-\alpha)/n)}[V^{3+}]^{-(1-n_k(1-\alpha)/n)}$. This rate law matches the positive order of V^{2+} and negative order of V^{3+} (with equal magnitude) observed in H_2SO_4, HCl, and HBr, indicating that V^{3+} adsorbs stronger than V^{2+} in these three electrolytes. However, at a given temperature, if $1 >> (K_1[V^{2+}] + K_3[V^{3+}])$, that is, both V^{2+} and V^{3+} adsorb weakly, $i_o \propto [V^{2+}]^{(1-(n_k(1-\alpha)/n))}[V^{3+}]^{(n_k(1-\alpha)/n)}$, explaining the positive reaction orders observed for both V^{2+} and V^{3+} in $HClO_4$ and HI ($\gamma, \varepsilon > 0$). The microkinetic model shows that the reaction kinetics is controlled by the V^{2+} and V^{3+} adsorption energies. With the reactant species in solution and reaction model identified, we next examine the energetics of adsorbed V complexes and anions using DFT.

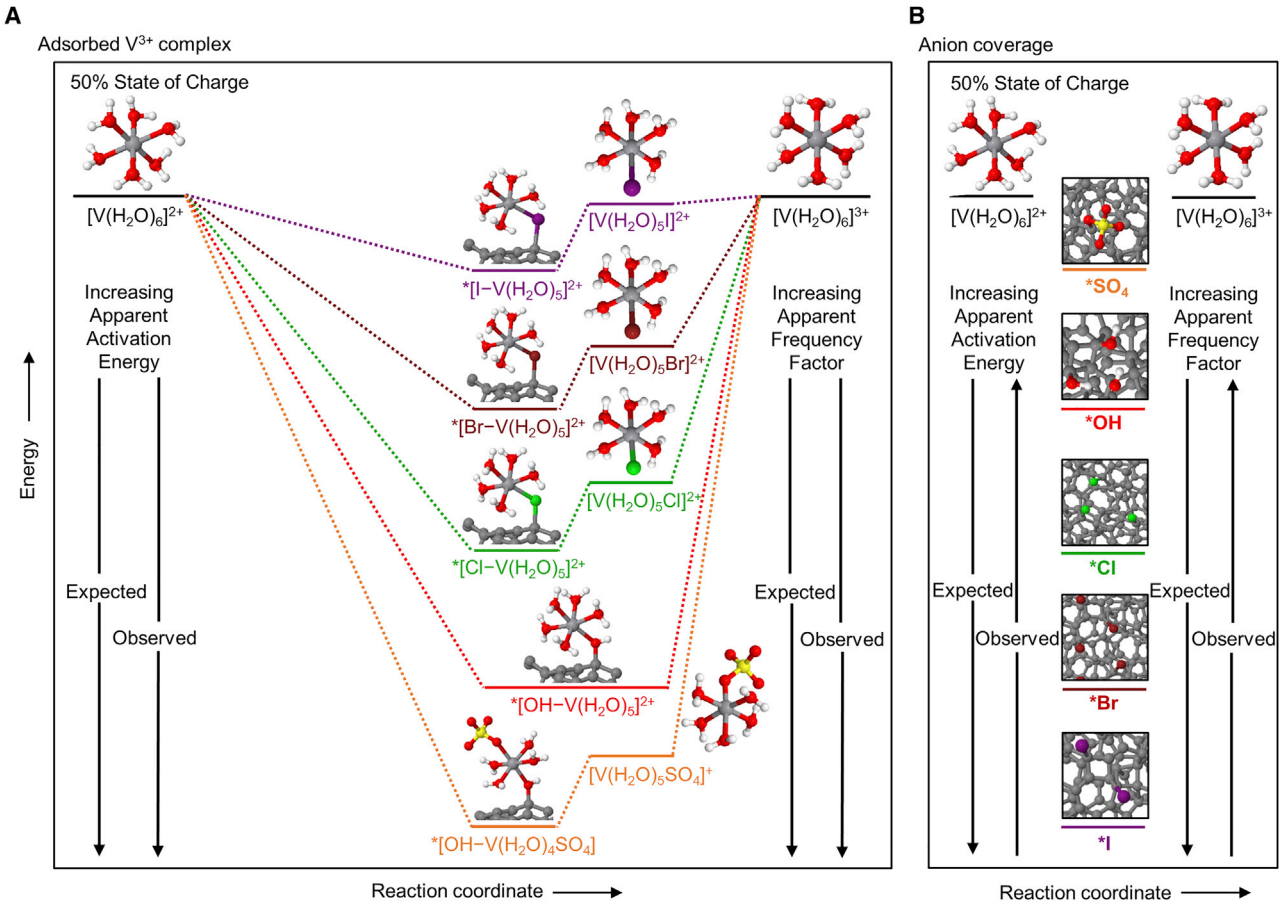

Scheme 2. Proposed Reaction Energy Diagram for the V^{2+}/V^{3+} Redox Reaction at 50% State of Charge and V^{2+}/V^{3+} Standard Redox Potential Considering Two Possible Mechanisms to Explain the Effect of Anions on Redox Kinetics

Adsorbed V^{3+} complex (i.e., *[bridge–V^{3+}]) as reaction intermediate (A) and anion coverage (i.e., *bridge) (B). For simplicity, the energy diagram is not drawn to scale and does not show balancing anions and electrons involved in the reaction. Black arrows point in the direction of increasing apparent activation energy and apparent frequency factor based on expected and observed behavior. We show $[V(H_2O)_5X]^{2+}$ (X = Cl, Br, I) as the species formed in solution for consistency. However, in actuality there would be a combination of both $[V(H_2O)_4X_2]^{+}$ and $[V(H_2O)_5X]^{2+}$ in solution. We expect the adsorbed intermediate to be closer to V^{3+} due to the easier desorption of V^{2+} than V^{3+}, as discussed in the main text. Atom color legend: light gray = V, red = O, white = H, green = chloride, brown = bromide, purple = iodide, and dark gray = GC.

Energies of V^{2+}/V^{3+} Complexes and Anions Adsorbed on GC

To explain whether the kinetic enhancement of the V^{2+}/V^{3+} reaction in the presence of different anions is explained by the energy of the adsorbed V intermediate (Scheme 1A) or anion coverage (Scheme 1B), we compare the predicted kinetic behavior based on DFT-calculated adsorption energies of V intermediates and anions with experimental observations. We demonstrate that the energy of the adsorbed V intermediate follows the same trend as anion polarizability and explains the trend in kinetic enhancement (Scheme 2A). We show that the coverage of adsorbed anions follows the opposite trend of our experimental measurements (Scheme 2B), and thus cannot explain the observed kinetic behavior.

DFT calculations predict the trend in energy of the adsorbed V^{3+} intermediate (i.e., *[bridge–V^{3+}]) on graphene matches the complexation strength of the free V^{3+} ion in solution. We calculate the energy of the *[bridge–V^{3+}] instead of *[bridge–V^{2+}] because barriers for desorption are higher for V^{3+} than V^{2+} with the OH bridge.[39,78] We assume that the desorption barrier is also higher for V^{3+}

than V^{2+} for other bridges. We use a graphene cluster model as a representative model for GC because of the challenges in accurately modeling amorphous surfaces (Supplemental Experimental Procedures). The adsorption strength of *[bridge−V^{3+}] (Figures S25 and S26) on graphene follows the order *[I−$V(H_2O)_5]^{2+}$ < *[Br−$V(H_2O)_5]^{2+}$ < *[Cl−$V(H_2O)_5]^{2+}$ < *[OH−$V(H_2O)_5]^{2+}$ < *[OH−$V(H_2O)_4SO_4$], reported in Table S12 and shown qualitatively in Scheme 2A, where weaker adsorption means a higher energy intermediate. The order of adsorption strength is the same for the di-halide V^{3+} complexes as for mono-halide V^{3+} complexes. The order of the adsorption strength of the *[bridge−V^{3+}] on graphene matches the ΔG_L of V^{3+} complex relative to $[V(H_2O)_6]^{3+}$ from our experimental UV-vis, DFT calculations, and the spectrochemical series.

The relative adsorption strength of *[bridge−V^{3+}] species rationalizes the observed kinetic behavior by Sabatier's principle,[79] which states that the adsorbed intermediate should bind with medium strength. Assuming the energy of the transition state shifts the same amount as the desorption energy of the intermediate by Brønsted-Evans-Polanyi relations,[80,81] the E_a would be lowered with the weakening of the adsorbed *[bridge−V^{3+}] intermediate. Weaker adsorption would also reduce the concentration of *[bridge−V^{3+}] on the surface, which would lower the apparent frequency factor. Based on the DFT-calculated adsorption free energy trends qualitatively shown in Scheme 2A, E_a and the apparent frequency factor for the V^{2+}/V^{3+} reaction should follow the order of I^- < Br^- < Cl^- < OH^- < SO_4^{2-} if the electron transfer step through adsorbed V acts as RDS, based on the rate law discussed above. This trend of E_a and apparent frequency factor with different anions matches the behavior observed in our experiments, which suggests that the energy of the *[bridge−V^{3+}] controls the V^{2+}/V^{3+} kinetics.

We propose that anion polarizability acts as a useful descriptor for the kinetics of the numerous redox couples involving 3*d* transition metal ions[23–26] because anion polarizability correlates with the energy of the adsorbed intermediate. The energy of the *[bridge−V^{3+}] in Scheme 2A follows the order of the anion polarizability. Consequently, the anion polarizability mimics the trends of observed V^{2+}/V^{3+} kinetics in different electrolytes.

The reaction pathway in Scheme 2A also captures the behavior of V^{2+}/V^{3+} reaction kinetics in mixtures of anions. The difference observed in kinetics in a mixture of I^- and SO_4^{2-} and kinetics with only I^-, $(i_{o,(I^- + SO_4^{2-})}/i_{o,I^-}) \approx 0.3$ (Figures 2 and S27A), implies that the V-sulfate intermediate is more energetically favorable than the V-iodide intermediate. In contrast, the kinetics with Cl^- are comparable in the presence and absence of SO_4^{2-} $(i_{o,(Cl^- + SO_4^{2-})}/i_{o,Cl^-}) \approx 0.9$ (Figures S11 and S27A). The smaller effect of sulfate on kinetics with Cl^- compared with I^- implies that the V-chloride intermediate is similar in energy to the V-sulfate intermediate (i.e., more favorable than the V-iodide intermediate). This order of energies qualitatively agrees with our calculations and is represented in Scheme 2A. Furthermore, the V^{2+}/V^{3+} kinetic behavior in mixtures of anions in the presence of sulfate also correlates with the difference in the ΔG_L of the V^{3+}-halide complexes relative to the V^{3+}-sulfate complex (Figure S27A). The more positive ΔG_L of V^{3+}-halide complexes relative to the V^{3+}-sulfate complex, the lower the concentration of reactive V^{3+}-halide complexes in solution, and the higher the relative inhibition in V^{2+}/V^{3+} reaction kinetics with SO_4^{2-}. The large apparent frequency factor in the presence of SO_4^{2-} ($\sim 10^6$) in comparison to other tested halides ($\sim 10^2$) (Figure S27B) also indicates that small concentrations of SO_4^{2-} will prevent the formation of active V^{3+}-halide complexes.

The relatively minor changes in i_o compared to the changes in the E_a can be explained by the adsorbed *[bridge−V^{3+}] intermediates representing only a small fraction of the surface sites. While the i_o varies at most by a factor of 15 throughout the electrolytes, the E_a decreases by ~30 kJ mol^{-1} at 50% SoC in HI compared to H_2SO_4. Such a significant decrease in E_a would imply a much larger increase in i_o, all else being equal. The total rate includes the contributions of reaction occurring both through the more active *[bridge−V^{3+}] intermediates on the surface and the less active sites comprising vacant C sites, carbonyl, and carboxyl groups on the surface.[27,47] Due to the weak adsorption on GC, the coverage of the active *[bridge−V^{3+}] intermediates on the surface remains low. Consequently, the portion of the reaction going through the more active *[bridge−V^{3+}] intermediates on the surface is small, rationalizing the minor increase in i_o. However, the E_a is dominated by the rapid charge transfer through the active *[bridge−V^{3+}] intermediates, explaining the large decline observed in E_a.

Our DFT calculations suggest that the increasing anion coverage, often considered as the reason for enhancement observed in the presence of anions for other transition metal ion redox couples,[23,50] does not explain the V^{2+}/V^{3+} reaction. The coverage (Figure S27B) and adsorption strength of anions at the equilibrium V^{2+}/V^{3+} redox potential on GC follow the order $I^- > Br^- > Cl^- > OH^- > SO_4^{2-}$. If the anion coverage controls the V^{2+}/V^{3+} reaction, as depicted in Scheme 2B, then the apparent frequency factor and E_a should increase with increasing anion adsorption strength, which is opposite to the experimentally observed behavior. This mismatch with the observed behavior allows us to conclude that anion coverages alone are not responsible for the observed kinetic trends. Also, the adsorption of SO_4^{2-} on GC is unfavorable with negligible coverage (Figure S27A), which suggests that SO_4^{2-} would not prevent I^- from adsorbing onto the electrode surface. Coverage calculations are discussed in Supplemental Experimental Procedures, with an accompanying discussion of Figures S28–S32 and Tables S13 and S14. These results do not mean that the reaction kinetics are not proportionally related to the coverage of a particular anion, but instead that the coverage is not the cause of the anion-enhancement trend observed here. Increasing the coverage of a particular anion enhances the reaction kinetics by increasing the concentration of that particular adsorbed V intermediate, as demonstrated in studies that oxidatively treat C electrodes and show improved V^{2+}/V^{3+} kinetics due to the increased coverage of OH groups.[47]

In conclusion, our results reveal how the structure of formed V complexes on the surface of GC influences kinetics for the V^{2+}/V^{3+} redox couple in five different acidic electrolytes. The energy of the formed *[bridge−V^{3+}] intermediate controls V^{2+}/V^{3+} kinetics and correlates with free anion polarizability. The anions enhance the kinetics by forming active *[bridge−V^{3+}] intermediates that have a lower activation barrier, rather than by increasing the coverage of the intermediates. These results can explain the similar kinetic trends observed for other redox couples involving 3*d* transition metal ions in the presence of anions, such as Cr^{2+}/Cr^{3+}, Fe^{2+}/Fe^{3+}, and Cu^{+}/Cu^{2+}, used for other RFBs. Our findings suggest that bridging anions may play a critical yet underexplored role in other RFB chemistries using transition metal ions for use in energy storage applications. The understanding of the structure of the adsorbed intermediate and its relation to the coverage and kinetics may lead to development of electrocatalysts that can adsorb V ions with the desired energy for improved kinetics. Recent studies have showcased the enormous potential of electrolyte engineering for Fe- and Cr-based RFBs,[9,82,83] in which chelating ligands are used to increase the faradaic efficiency and widen the operating voltage window of the battery. Knowledge gained from this study can be exploited in electrolyte

engineering or electrocatalyst development to tune the intermediate adsorption strength and control charge transfer kinetics. These findings will assist researchers in predicting and controlling the charge transfer kinetics of inner-sphere transition metal ion redox couples in the aqueous phase involved in other electrochemical applications.

EXPERIMENTAL PROCEDURES

Resource Availability

Lead Contact

Further information requests should be directed to the Lead Contact, Dr. Nirala Singh (snirala@umich.edu).

Materials Availability

This study did not generate new unique materials

Data and Code Availability

The authors declare that the data supporting the findings of this study are available within the article and the Supplemental Information. All other data are available from the Lead Contact upon reasonable request.

Description of Methods

See Supplemental Experimental Procedures for "Experimental Procedures," "Developing a Rate Law for V^{2+}/V^{3+} Reaction," "Molecular Dynamics Simulations for Extended X-ray Absorption Fine Structure (EXAFS) for V^{2+} and V^{3+} Complexes," "EXAFS to Identify Structures of V^{2+} and V^{3+} in Different Electrolytes," "Ligand Exchange Free Energies for V^{2+}/V^{3+} Complexes," "DFT Modeling of Adsorbed Intermediates," "Understanding Energetics of V^{3+} Complexes in Solution and Anions Adsorbed on Glassy Carbon," "Coverage of Anions on Glassy Carbon," and "Ruling Out Bi(sulfate) Surface Poisoning."

SUPPLEMENTAL INFORMATION

Supplemental Information can be found online at https://doi.org/10.1016/j.xcrp.2020.100307.

ACKNOWLEDGMENTS

We would like to thank John Fulton and Mahalingam Balasubramanian for their help in conducting and fitting the EXAFS measurements. We also thank Niri Govind and Eric Bylaska for their insights in using NWChem to study the adsorption of V complexes. This research is funded by University of Michigan Office of Research grant no. UMOR-29814. This research used the resources of the National Energy Research Scientific Computing Center (NERSC), a US DOE Office of Science User Facility operated under contract no. DE-AC02-05CH11231. This research used resources of the Advanced Photon Source Sector 20, a US DOE Office of Science User Facility operated for the DOE Office of Science by Argonne National Laboratory under contract no. DE-AC02-06CH11357, and the Canadian Light Source and its funding partners.

AUTHOR CONTRIBUTIONS

N.S. conceived the project. H.A. and N.S. designed all of the experiments. H.A. conducted all of the experiments and analyzed the data under the guidance of N.S. J.F. did the MD-EXAFS and DFT calculations under the guidance of B.R.G. The manuscript was written through the contributions of all authors. All authors have given approval to the final version of the manuscript.

DECLARATION OF INTERESTS

The authors declare no competing interests.

Received: September 2, 2020
Revised: December 2, 2020
Accepted: December 10, 2020
Published: January 20, 2021

REFERENCES

1. Newman, R.C., and Sieradzki, K. (1994). Metallic corrosion. Science *263*, 1708–1709.

2. Jeon, B., Sankaranarayanan, S.K.R.S., van Duin, A.C.T., and Ramanathan, S. (2011). Atomistic insights into aqueous corrosion of copper. J. Chem. Phys. *134*, 234706.

3. Frankel, G.S. (1998). Pitting Corrosion of Metals: A Review of the Critical Factors. J. Electrochem. Soc. *145*, 2186–2198.

4. Bhat, M.A., Nioradze, N., Kim, J., Amemiya, S., and Bard, A.J. (2017). In Situ Detection of the Adsorbed Fe(II) Intermediate and the Mechanism of Magnetite Electrodeposition by Scanning Electrochemical Microscopy. J. Am. Chem. Soc. *139*, 15891–15899.

5. Gimenez-Romero, D., Juan García-Jareño, J., Agrisuelas, J., Gabrielli, C., Perrot, H., and Vicente, F. (2008). Formation of a Copper Oxide Layer as a Key Step in the Metallic Copper Deposition Mechanism. J. Phys. Chem. C *112*, 4275–4280.

6. Morales-Guio, C.G., Liardet, L., and Hu, X. (2016). Oxidatively Electrodeposited Thin-Film Transition Metal (Oxy)hydroxides as Oxygen Evolution Catalysts. J. Am. Chem. Soc. *138*, 8946–8957.

7. Iovan, D.A., Jia, S., and Chang, C.J. (2019). Inorganic Chemistry Approaches to Activity-Based Sensing: From Metal Sensors to Bioorthogonal Metal Chemistry. Inorg. Chem. *58*, 13546–13560.

8. Asl, H.Y., and Manthiram, A. (2020). Reining in dissolved transition-metal ions. Science *369*, 140–141.

9. Robb, B.H., Farrell, J.M., and Marshak, M.P. (2019). Chelated Chromium Electrolyte Enabling High-Voltage Aqueous Flow Batteries. Joule *3*, 2503–2512.

10. Luo, J., Hu, B., Debruler, C., Bi, Y., Zhao, Y., Yuan, B., Hu, M., Wu, W., and Liu, T.L. (2019). Unprecedented Capacity and Stability of Ammonium Ferrocyanide Catholyte in pH Neutral Aqueous Redox Flow Batteries. Joule *3*, 149–163.

11. i3. Electrochemical Storage: Investment and Innovation Trends, Top Deals and Deal-Makers. https://i3connect.com/tags/electrochemical-storage/899/activity.

12. US Energy Information Administration (2019). DOE-EIA International Energy Outlook 2019. https://www.eia.gov/pressroom/presentations/capuano_09242019.pdf.

13. Nguyen, T., and Savinell, R.F. (2010). Flow Batteries. Electrochem. Soc. Interface *19*, 54–56.

14. Dunn, B., Kamath, H., and Tarascon, J.-M. (2011). Electrical energy storage for the grid: a battery of choices. Science *334*, 928–935.

15. Thaller, L.H. (1974). Electrically Rechargeable Redox Flow Cells. In Proceedings of the 9th Intersociety Energy Conversion Engineering Conference (A75-10476 01-44) (American Society of Mechanical Engineers), pp. 924–928.

16. Sanz, L., Lloyd, D., Magdalena, E., Palma, J., and Kontturi, K. (2014). Description and Performance of a Novel Aqueous All-Copper Redox Flow Battery. J. Power Sources *268*, 121–128.

17. Kocyigit, N., Gencten, M., Sahin, M., and Sahin, Y. (2020). A Novel Vanadium/Cobalt Redox Couple in Aqueous Acidic Solution for Redox Flow Batteries. Int. J. Energy Res. *44*, 411–424.

18. Cheng, J., Zhang, L., Yang, Y.-S., Wen, Y.-H., Cao, G.-P., and Wang, X.-D. (2007). Preliminary Study of Single Flow Zinc-Nickel Battery. Electrochem. Commun. *9*, 2639–2642.

19. Rubio-Garcia, J., Kucernak, A., Zhao, D., Li, D., Fahy, K., Yufit, V., Brandon, N., and Gomez-Gonzalez, M. (2019). Hydrogen/Manganese Hybrid Redox Flow Battery. J. Phys. Energy *1*, 015006.

20. Dong, Y.R., Kaku, H., Hanafusa, K., Moriuchi, K., and Shigematsu, T. (2015). A Novel Titanium/Manganese Redox Flow Battery. ECS Trans. *69*, 59–67.

21. Henstridge, M.C., Laborda, E., Rees, N.V., and Compton, R.G. (2012). Marcus-Hush-Chidsey Theory of Electron Transfer Applied to Voltammetry: A Review. Electrochim. Acta *84*, 12–20.

22. Kim, K.J., Park, M.-S., Kim, Y.-J., Kim, J.H., Dou, S.X., and Skyllas-Kazacos, M. (2015). A Technology Review of Electrodes and Reaction Mechanisms in Vanadium Redox Flow Batteries. J. Mater. Chem. A Mater. Energy Sustain. *3*, 16913–16933.

23. Aikens, D.A., and J.W.R., , Jr.. (1961). Effect of Chloride on the Kinetics of Electroöxidation of Chromium (II) in Acidic Perchlorate Medium. J. Phys. Chem. *65*, 1213–1216.

24. Rodes, A., Feliu, J.M., Aldaz, A., and Clavilier, J. (1989). The Influence of Polyoriented Gold Electrodes Modified by Reversibly and Irreversibly Adsorbed Ad-atoms on the Redox Behaviour of the Cr(III)/Cr(II) Couple and the Effect of Chloride Ions. J. Electroanal. Chem *271*, 127–139.

25. Weber, J., Samec, Z., and Mareček, V. (1978). The Effect of Anion Adsorption on the Kinetics of the Fe^{3+}/Fe^{2+} Reaction on Pt and Au Electrodes in $HClO_4$. J. Electroanal. Chem. Interfacial Electrochem. *89*, 271–288.

26. Nagy, Z., Blaudeau, J.P., Hung, N.C., Curtiss, L.A., and Zurawski, D.J. (1995). Chloride Ion Catalysis of the Copper Deposition Reaction. J. Electrochem. Soc. *142*, L87–L89.

27. Fink, H., Friedl, J., and Stimming, U. (2016). Composition of the Electrode Determines Which Half-Cell's Rate Constant is Higher in a Vanadium Flow Battery. J. Phys. Chem. C *120*, 15893–15901.

28. Aaron, D., Sun, C.-N., Bright, M., Papandrew, A.B., Mench, M.M., and Zawodzinski, T.A. (2013). In Situ Kinetics Studies in All-Vanadium Redox Flow Batteries. ECS Electrochem. Lett. *2*, A29–A31.

29. Bourke, A., Miller, M.A., Lynch, R.P., Gao, X., Landon, J., Wainright, J.S., Savinell, R.F., and Buckley, D.N. (2016). Electrode Kinetics of Vanadium Flow Batteries: Contrasting Responses of V^{II}-V^{III} and V^{IV}-V^{V} to Electrochemical Pretreatment of Carbon. J. Electrochem. Soc. *163*, A5097–A5105.

30. Pour, N., Kwabi, D.G., Carney, T., Darling, R.M., Perry, M.L., and Shao-Horn, Y. (2015). Influence of Edge-and Basal-Plane Sites on the Vanadium Redox Kinetics for Flow Batteries. J. Phys. Chem. C *119*, 5311–5318.

31. Ventosa, E., Skoumal, M., Vázquez, F.J., Flox, C., and Morante, J.R. (2014). Operando Studies of All-Vanadium Flow Batteries: Easy-to-Make Reference Electrode Based on Silver-Silver Sulfate. J. Power Sources *271*, 556–560.

32. Liu, M., Xiang, Z., Deng, H., Wan, K., Liu, Q., Piao, J., Zheng, Y., and Liang, Z. (2016). Electrochemical Behavior of Vanadium Redox Couples on Carbon Electrode. J. Electrochem. Soc. *163*, H937–H942.

33. Wei Wu, X., Yamamura, T., Ohta, S., Xiu Zhang, Q., Cong Lv, F., Ming Liu, C., Shirasaki, K., Satoh, I., Shikama, T., Lu, D., et al. (2011). Acceleration of the Redox Kinetics of VO^{2+}/VO_2^+ and V^{3+}/V^{2+} Couples on Carbon Paper. J. Appl. Electrochem. *41*, 1183–1190.

34. Zhang, M., Moore, M., Watson, J.S., Zawodzinski, T.A., and Counce, R.M. (2012). Capital Cost Sensitivity Analysis of an All-Vanadium Redox-Flow Battery. J. Electrochem. Soc. *159*, 1183–1188.

35. Dmello, R., Milshtein, J.D., Brushett, F.R., and Smith, K.C. (2016). Cost-Driven Materials Selection Criteria for Redox Flow Battery Electrolytes. J. Power Sources *330*, 261–272.

36. Roznyatovskaya, N., Noack, J., Mild, H., Fühl, M., Fischer, P., Pinkwart, K., Tübke, J., and

Skyllas-Kazacos, M. (2019). Vanadium Electrolyte for All-Vanadium Redox-Flow Batteries: The Effect of the Counter Ion. Batteries *5*, 13.

37. Ding, C., Zhang, H., Li, X., Liu, T., and Xing, F. (2013). Vanadium Flow Battery for Energy Storage: Prospects and Challenges. J. Phys. Chem. Lett. *4*, 1281–1294.

38. Skyllas-Kazcos, M. (2019). Performance Improvements and Cost Considerations of the Vanadium Redox Flow Battery. ECS Trans. *89*, 29–45.

39. Rodby, K.E., Carney, T.J., Ashraf Gandomi, Y., Barton, J.L., Darling, R.M., and Brushett, F.R. (2020). Assessing the Levelized Cost of Vanadium Redox Flow Batteries with Capacity Fade and Rebalancing. J. Power Sources *460*, 227958.

40. Kim, S., Vijayakumar, M., Wang, W., Zhang, J., Chen, B., Nie, Z., Chen, F., Hu, J., Li, L., and Yang, Z. (2011). Chloride supporting electrolytes for all-vanadium redox flow batteries. Phys. Chem. Chem. Phys. *13*, 18186–18193.

41. Skyllas-Kazacos, M. (2003). Novel Vanadium Chloride/Polyhalide Redox Flow Battery. J. Power Sources *124*, 299–302.

42. Wang, W., Kim, S., Chen, B., Nie, Z., Zhang, J., Xia, G.-G., Li, L., and Yang, Z. (2011). A New Redox Flow Battery Using Fe/V Redox Couples in Chloride Supporting Electrolyte. Energy Environ. Sci. *4*, 4068–4073.

43. Wang, W., Nie, Z., Chen, B., Chen, F., Luo, Q., Wei, X., Xia, G.G., Skyllas-Kazacos, M., Li, L., and Yang, Z. (2012). A New Fe/V Redox Flow Battery Using a Sulfuric/Chloric Mixed-Acid Supporting Electrolyte. Adv. Energy Mater. *2*, 487–493.

44. Li, L., Kim, S., Wang, W., Vijayakumar, M., Nie, Z., Chen, B., Zhang, J., Xia, G., Hu, J., Graff, G., et al. (2011). A Stable Vanadium Redox-Flow Battery with High Energy Density for Large-Scale Energy Storage. Adv. Energy Mater. *1*, 394–400.

45. Skyllas-Kazacos, M., Cao, L., Kazacos, M., Kausar, N., and Mousa, A. (2016). Vanadium Electrolyte Studies for the Vanadium Redox Battery-A Review. ChemSusChem *9*, 1521–1543.

46. Agarwal, H., Florian, J.R., Goldsmith, B., and Singh, N. (2019). V^{2+}/V^{3+} Redox Kinetics on Glassy Carbon in Acidic Electrolytes for Vanadium Redox Flow Batteries. ACS Energy Lett. *4*, 2368–2377.

47. Li, Y., Parrondo, J., Sankarasubramanian, S., and Ramani, V. (2019). Impact of Surface Carbonyl-and Hydroxyl-Group Concentrations on Electrode Kinetics in an All-Vanadium Redox Flow Battery. J. Phys. Chem. C *123*, 6370–6378.

48. Sun, B., and Skyllas-Kazacos, M. (1992). Chemical Modification of Graphite Electrode Materials for Vanadium Redox Flow Battery Application—Part II. Acid Treatments. Electrochim. Acta *37*, 2459–2465.

49. Jiang, Z., Klyukin, K., and Alexandrov, V. (2017). First-principles study of adsorption-desorption kinetics of aqueous V^{2+}/V^{3+} redox species on graphite in a vanadium redox flow battery. Phys. Chem. Chem. Phys. *19*, 14897–14901.

50. de Levie, R. (1971). Anion Bridging and Anion Electrocatalysis on Mercury. J. Electrochem. Soc. *118*, 185C–192C.

51. Anbar, M., and Hart, E.J. (1965). The Reactivity of Metal Ions and Some Oxy Anions toward Hydrated Electrons. J. Phys. Chem. *69*, 973–977.

52. Heyrovský, J. (1947). Retarded Electrodeposition of Metals Studied Oscillographically with Mercury Capillary Electrodes. Discuss. Faraday Soc. *1*, 212–225.

53. Sykes, A.G. (1968). Further Advances in the Study of Mechanisms of Redox Reactions. Adv. Inorg. Chem. Radiochem. *10*, 153–245.

54. Nagle, J.K. (1990). Atomic Polarizability and Electronegativity. J. Am. Chem. Soc. *112*, 4741–4747.

55. Hati, S., and Datta, D. (1995). Electronegativity and Static Electric Dipole Polarizability of Atomic Species. A Semiempirical Relation. J. Phys. Chem. *99*, 10742–10746.

56. Yee Leung, K., and McCrory, C.C.L. (2019). Effect and Prevention of Trace Ag^{+} Contamination from Ag/AgCl Reference Electrodes on CO_2 Reduction Product Distributions at Polycrystalline Copper Electrodes. ACS Appl. Energy Mater. *2*, 8283–8293.

57. Newton, T.W., and Baker, F.B. (1964). The Intermediate in the Reaction between Vanadium(II) and Vanadium(IV). Inorg. Chem. *3*, 569–573.

58. Ribas Gispert, J. (2008). Coordination Chemistry, First Edition (Wiley-VCH).

59. Scott, S.L. (2019). The Burden of Disproof. ACS Catal. *9*, 4706–4708.

60. Palmer, B.J., Pfund, D.M., and Fulton, J.L. (1996). Direct Modeling of EXAFS Spectra from Molecular Dynamics Simulations. J. Phys. Chem. *100*, 13393–13398.

61. Richens, D.T. (1997). Group 5 Elements: Vanadium, Niobium and Tantalum. The Chemistry of Aqua Ions: Synthesis, Structure and Reactivity (John Wiley & Sons), pp. 230–235.

62. Sepehr, F., and Paddison, S.J. (2013). The Solvation Structure and Thermodynamics of Aqueous Vanadium Cations. Chem. Phys. Lett. *585*, 53–58.

63. Krakowiak, J., Lundberg, D., and Persson, I. (2012). A coordination chemistry study of hydrated and solvated cationic vanadium ions in oxidation states +III, +IV, and +V in solution and solid state. Inorg. Chem. *51*, 9598–9609.

64. Cotton, F.A., Falvello, L.R., Llusar, R., Libby, E., Murillo, C.A., and Schwotzer, W. (1986). Synthesis and Characterization of Four Vanadium(II) Compounds, Including Vanadium(II) Sulfate Hexahydrate and Vanadium(II). Saccharinates. Inorg. Chem. *25*, 3423–3428.

65. Cotton, F.A., Fair, C.K., Lewis, G.E., Mott, G.N., Ross, F.K., Schultz, A.J., and Williams, J.M. (1984). Precise Structural Characterizations of the Hexaaquovanadium(III) and Diaquohydrogen Ions. X-ray and Neutron Diffraction Studies of $[V(H_2O)_6][H_5O_2](CF_3SO_3)_4$. J. Am. Chem. Soc. *106*, 5319–5323.

66. Cotton, F.A., Falvello, L.R., Murillo, C.A., Pascual, I., Schultz, A.J., and Tomás, M. (1994). Neutron and X-ray Structural Characterization of the Hexaaquavanadium(II) Compound $VSO_4.7H_2O$. Inorg. Chem. *33*, 5391–5395.

67. Fulton, J.L., Bylaska, E.J., Bogatko, S., Balasubramanian, M., Cauët, E., Schenter, G.K., and Weare, J.H. (2012). Near-Quantitative Agreement of Model-Free DFT-MD Predictions with XAFS Observations of the Hydration Structure of Highly Charged Transition-Metal Ions. J. Phys. Chem. Lett. *3*, 2588–2593.

68. Bon, M., Laino, T., Curioni, A., and Parrinello, M. (2016). Characterization of Vanadium Species in Mixed Chloride−Sulfate Solutions: An Ab Initio Metadynamics Study. J. Phys. Chem. C *120*, 10791–10798.

69. Vijayakumar, M., Li, L., Nie, Z., Yang, Z., and Hu, J. (2012). Structure and stability of hexa-aqua V(III) cations in vanadium redox flow battery electrolytes. Phys. Chem. Chem. Phys. *14*, 10233–10242.

70. Gupta, S., Lim, T.M., and Mushrif, S.H. (2018). Insights into the Solvation of Vanadium Ions in the Vanadium Redox Flow Battery Electrolyte Using Molecular Dynamics and Metadynamics. Electrochim. Acta *270*, 471–479.

71. Oldenburg, F.J., Bon, M., Perego, D., Polino, D., Laino, T., Gubler, L., and Schmidt, T.J. (2018). Revealing the role of phosphoric acid in all-vanadium redox flow batteries with DFT calculations and in situ analysis. Phys. Chem. Chem. Phys. *20*, 23664–23673.

72. Martin. Ernest, L., and Bentley, K.E. (1962). Spectrophotometric Investigation of Vanadium(II), Vanadium(III), and Vanadium(IV) in Various Media. Anal. Chem. *34*, 354–358.

73. Landry-Hum, J., Bussière, G., Daniel, C., and Reber, C. (2001). Triplet electronic states in $d^{(2)}$ and $d^{(8)}$ complexes probed by absorption spectroscopy: a CASSCF/CASPT2 analysis of $[V(H_2O)_6]^{3+}$ and $[Ni(H_2O)_6]^{2+}$. Inorg. Chem. *40*, 2595–2601.

74. Bussière, G., Beaulac, R., Cardinal-David, B., and Reber, C. (2001). Coupled Electronic States in *trans*-$MCl_2(H_2O)_4^{n+}$ Complexes (M: Ni^{2+}, Co^{2+}, V^{3+}, Cr^{3+}) Probed by Absorption and Luminescence Spectroscopy. Coord. Chem. Rev. *219–221*, 509–543.

75. Frank, P., Kustin, K., Robinson, W.E., Linebaugh, L., and Hodgson, K.O. (1995). Nature and Ligation of Vanadium within Whole Blood Cells and Henze Solution from the Tunicate Ascidia ceratodes, As Investigated by Using X-ray Absorption Spectroscopy. Inorg. Chem. *34*, 5942–5949.

76. Chandrasekhar, P., and Bird, P.H. (1984). Synthesis and Characterization of an Oxygen-Bridged Vanadium(III). Dimer. Inorg. Chem. *23*, 3677–3679.

77. Hedman, B., Sung Co, M., Armstrong, W.H., Hodgson, K.O., and Lippard, S.J. (1986). EXAFS Studies of Binuclear Iron Complexes as Models for Hemerythrin and Related Proteins. Inorg. Chem. *25*, 3708–3711.

78. Jiang, Z., and Alexandrov, V. (2020). Electrocatalytic Activity of Oxygen-Functionalized Carbon Electrodes for Vanadium Redox Flow Batteries from Free-Energy Calculations. ACS Appl. Energy Mater. *3*, 7543–7549.

79. Nørskov, J.K., Studt, F., Abild-Pedersen, F., and Bligaard, T. (2014). Fundamental Concepts in Heterogeneous Catalysis (John Wiley & Sons).

80. Nørskov, J.K., Bligaard, T., Logadottir, A., Bahn, S., Hansen, L.B., Bollinger, M., Bengaard, H., Hammer, B., Sljivancanin, Z., Mavrikakis, M., et al. (2002). Universality in Heterogeneous Catalysis. J. Catal. *209*, 275–278.

81. Bligaard, T., Nørskov, J.K., Dahl, S., Matthiesen, J., Christensen, C.H., and Sehested, J. (2004). The Brønsted-Evans-Polanyi Relation and the Volcano Curve in Heterogeneous Catalysis. J. Catal. *224*, 206–217.

82. Ruan, W., Mao, J., Yang, S., Shi, C., Jia, G., and Chen, Q. (2020). Designing Cr complexes for a neutral Fe-Cr redox flow battery. Chem. Commun. (Camb.) *56*, 3171–3174.

83. Waters, S.E., Robb, B.H., and Marshak, M.P. (2020). Effect of Chelation on Iron–Chromium Redox Flow Batteries. ACS Energy Lett. *5*, 1758–1762.